Geochemistry, Geophysics, Geosystems

Supporting Information for

Hydrous Regions of the Mantle Transition Zone Lie Beneath Areas of Continental Intraplate Volcanism

Helene Wang[1,2], Valentina Magni[1,3], Clinton P. Conrad[1,4,*] and Mathew Domeier[1,4]

[1] Centre for Earth Evolution and Dynamics (CEED), University of Oslo, Oslo, Norway

[2] TGS, Oslo, Norway

[3] Norwegian Geotechnical Institute (NGI), Oslo, Norway

[4] Centre for Planetary Habitability (PHAB), University of Oslo, Oslo, Norway

[*] Corresponding author: Clinton P. Conrad (c.p.conrad@geo.uio.no)

Contents of this file

Text S1. Computing the Regassing Flux from the Tectonic Plate Reconstruction

We follow the approach of *Karlsen et al.* [2019] to compute regassing rates from the tectonic reconstruction of *Matthews et al.* [2016], which has been corrected as described by *Torsvik et al.* [2019]. For each plate boundary segment that is identified as a subduction zone, we compute the mass of slab material subducted per unit time:

$$\frac{dM_l}{dt} = \rho v_s d L_s \qquad \text{(S1)}$$

where ρ, v_s, d, and L_s are the density, convergence velocity, thickness, and length of the subduction zone segment, respectively. We use a plate density of ρ=3200 kg/m^3. To find the regassing rate of the segment, we multiply equation S1 by the nondimensional regassing factor α (described below), which describes the mass of subducting water as a fraction of the mass of the slab. Because most of this water is degassed through a volcanic arc, we also multiply by a fraction ε (described below), which *Karlsen et al.* [2019] defined as the fraction of the subducted water that descends into the deep mantle. The regassing water flux (R) is thus:

$$R = \alpha \varepsilon \rho v_s d L_s \qquad \text{(S2)}$$

The thickness *d* of the subducting slab depends on the age τ of the oceanic lithosphere:

$$d(\tau) = 2.32\sqrt{\kappa\tau} \qquad \text{(S3)}$$

where 80 Myr > τ > 10 Myr and $\kappa = 7.6 \cdot 10^{-7}$ m^2/s is the thermal diffusivity. For τ > 80 Myr and τ < 10 Myr, upper and lower bounds on plate thickness are set to 100 km and 36 km, respectively [*Sclater et al.*, 1980]. We applied a minimum velocity limit of 0.2 cm/yr to exclude inactive plate boundaries. This filtering mainly affects the total length of subduction zones, and does not significantly affect the total area of subducted seafloor [*Karlsen et al.*, 2019] because only inactive or very slowly converging trenches are removed. While both continental and oceanic subduction zones are included, any convergent boundaries that are not explicitly identified as a subduction zone in the tectonic reconstruction model (e.g., continental convergence) are ignored.

The nondimensional regassing factor α relates to the slab's initial bulk water content, and is a poorly constrained parameter [*Karlsen et al.*, 2019]. We chose a constant value of $\alpha = 2.28\times10^{-3}$ [*Karlsen et al.*, 2019] , which yields a present-day global H_2O subduction flux of $3.44 \cdot 10^{11}$ kg/yr to depths > 230 km. This flux is within the range estimated by *van Keken et al.* [2011] and describes the "regassing-dominated" case of *Karlsen et al.* [2019]. Other studies have estimated both smaller [*Bodnar et al.*, 2013; *Faccenda et al.*, 2012; *Parai and Mukhopadhyay*, 2012; *Rüpke et al.*, 2004] or larger [*Hacker*, 2008; *Magni et al.*, 2014] regassing fluxes for the present Earth. We note that the choice of regassing factor mostly affects the magnitude of water content within the transition zone, and not lateral variations in the heterogeneous distribution of water in the mantle.

The water retention factor ε expresses the fraction of the initial water content of the slab that reaches the deep mantle (below 410 km depth). Because colder and faster slabs remain colder at depth, and therefore can retain more water [*Magni et al.*, 2014; *Rüpke et al.*, 2004; *van Keken et al.*, 2011], this factor depends on the thermal parameter $\Phi = v_s\tau$ of each specific subduction zone segment. *Karlsen et al.* [2019] expressed the water retention factor as $\varepsilon(\Phi) = max\left(0, a + b(1 - e^{-c\Phi})\right)$, and determined the constants *a*, *b* and *c* by fitting the function $\varepsilon(\Phi)$ to an independent study of slab water retention [*Rüpke et al.*, 2004]. Here we use $a = -0.1$, $b = 0.5$, and $c = 0.0023$, as given by *Karlsen et al.* [2019] to compute $\varepsilon(\Phi)$. Our regassing estimates thus account for an increase in slab water content with seafloor age, via the thermal parameter, but we ignore other lateral or temporal dependencies (e.g., those based on variations in plate bending, sediment accumulation or other heterogeneities). We note that water contained within the shallow parts of the plate, such as within the crust or accumulated sediments, probably contributes little to regassing because these regions become significantly dehydrated by heating as the slab descends [*Rüpke et al.*, 2004; *van Keken et al.*, 2011].

We computed ε for all individual subduction zone segments, for all times $t \in [0,400]$, and found that global mean values of ε vary between about 0.1 and 0.25, with a mean value of about 0.14 for the present day (Figure S1c). These values result in large variations in regassing rates, which range from about $0.35 \cdot 10^{12}$ kg/yr for the present day to more than $1.5 \cdot 10^{12}$ kg/yr at 125 Ma (Figure S1e). Regional variations in the rate of water input into the mantle are significant, with older and faster slabs bringing water downward more rapidly (main text Figure 2, left column).

Text S2. Distributing Regassed Water onto MTZ Grid Points

Regassed water from subduction is distributed within the MTZ onto a global mesh of grid points (Figure S2, left). Each mesh point represents approximately 50000 km^2 on the Earth's surface (~225 km spacing),

or ~40000 km^2 at the base of the MTZ. We distributed water from each segment among the *N* nearest neighbor points around its segment midpoint (Figure S2, right). The amount of water added to each k^{th} nearest neighbor mesh point is weighted by the distance from the segment midpoint. If d_k is the distance to the k^{th} nearest neighbor mesh point, then that point receives a fraction of water given by $\frac{D}{d_k}$ where $D = 1/\left(\sum_{i=1}^{N} \frac{1}{d_i}\right)$. Then the total water assigned to this point is:

$$M_k = \frac{R}{A} \Delta t \frac{\mathrm{D}}{d_k} \qquad \text{(S4)}$$

where M_k, *R*, *A*, and *Δt* are the water mass per area assigned to mesh point *k*, the regassing flux of the subduction segment (equation S2), the mesh point surface area, and the time step (i.e., 1 Myr). We found in tests that increasing *N* from 10 to 30, which increases the lateral spread of water from 390 km to 690 km, increases the fraction of "wet" grid points (defined using a threshold of 0.5·10^9 kg/km^2, see section 2.3) by less than 20% (Figure 7 of *Wang* [2022]). Thus, the effect of the choice of *N* is modest, and we use *N*=10 in this study. We note that the lateral spread of the water in the MTZ is more closely related to slab stagnation (Figure 5a of the main text). We thus account for slab stagnation by applying an MTZ residence time t_{MTZ}, and using a constant value of *N*=10 to distribute water within ~390 km of each subduction zone midpoint (Figure S2).

Text S3. Developing the Continental Intraplate Volcanism (IPV) Database

Using the criteria described in the main text, we extracted 2096 locations of continental IPV (Figure S3a) from the GEOROC (https://georoc.eu/) database [*Lehnert et al.*, 2000], after removing all duplicate points. Each location has a specified age range during which IPV was active. For example, 468 locations indicate currently active IPV samples with an age of 0 Ma (Figure S3b). For earlier times, we reconstructed the eruption locations of active IPV by applying the GPlates [*Müller et al.*, 2018] continent polygon files from the tectonic reconstruction of *Matthews et al.* [2016], corrected as described by *Torsvik et al.* [2019]. By assigning each previously-active IPV point to a continental polygon, itself associated with a representative plate (i.e., its PlateID), the IPV points are rotated, along with their continental polygons, back to their locations at the time of eruption. Typically, samples are defined using an age range, instead of a specific eruption time. We reconstruct these IPV points backward onto maps for each 1 Myr age increment within the point's given age range. For a few points, this age range was limited by the age range of the continental polygon associated with the IPV point.

We note that many IPV observations are positioned in the near vicinity of each other (with a spacing closer than our grid spacing of ~225 km), and are likely associated with the same volcanic eruption. Thus, where several IPV points are associated with the same mesh point on a given age map, we merged the cluster into one single point with the coordinates of the mesh point (Figure S3b). The above exclusions narrow the number of present-day active intraplate volcanic samples to 132 (Figures 2l and 3f of the main text). This filtering has been applied to each timestep in the considered time range (main text Figure 2, right column), resulting in a changing number of IPV points for each timestep (Figure S3c). Because many samples are defined using an age range, we find extended periods with a relatively constant number of IPV samples, broken by jumps in the number of samples. The number of IPV data points is smaller in the past because the geologic record of IPV becomes increasingly erased backward in time.

Text S4. Constructing Random Rotations of the MTZ Hydration Maps

We generated random rotations following the approach of *Miles* [1965], who showed that a uniform distribution of rotation poles on the Earth's surface, coupled with rotation angles drawn from the distribution $(\theta - sin\theta)/\pi$ (where $0 \leq \theta \leq \pi$), produces a uniform distribution of random re-orientations. Thus, an object on Earth's surface (e.g., an MTZ hydration map) can be randomly-reoriented to a new position on Earth's surface using this procedure.

Although we compare MTZ hydration to IPV locations only on continents, we randomly rotate the entire MTZ grid, including both oceanic and continental regions. If we had excluded the oceanic regions (where we have no IPV locations), we would reduce the wet MTZ area by more than half (Figure S6). In that case, any random rotation that positions formerly oceanic MTZ beneath continental areas would show a poor comparison to IPV simply for geometrical reasons. By rotating the entire MTZ grid, we consider the placement of all continental IPV locations relative to the entire distribution of hydrated MTZ.

We show a few examples of randomly re-oriented MTZ hydration maps, and their correlations with (unrotated) IPV, in Figure S7.

References

Bodnar, R. J., T. Azbej, S. P. Becker, C. Cannatelli, A. Fall, and M. J. Severs (2013), Whole Earth geohydrologic cycle, from the clouds to the core: The distribution of water in the dynamic Earth system, *Geological Society of America Special Papers*, *500*, 431-461. https://doi.org/10.1130/2013.2500(13)

Faccenda, M., T. V. Gerya, N. S. Mancktelow, and L. Moresi (2012), Fluid flow during slab unbending and dehydration: Implications for intermediate-depth seismicity, slab weakening and deep water recycling, *Geochem. Geophys. Geosyst.*, *13*, Q01010. https://doi.org/10.1029/2011gc003860

Hacker, B. R. (2008), H2O subduction beyond arcs, *Geochem. Geophys. Geosyst.*, *9*(3), Q03001. https://doi.org/10.1029/2007gc001707

Karlsen, K. S., C. P. Conrad, and V. Magni (2019), Deep Water Cycling and Sea Level Change Since the Breakup of Pangea, *Geochemistry, Geophysics, Geosystems*, *20*(6), 2919-2935. https://doi.org/10.1029/2019GC008232

Lehnert, K., Y. Su, C. H. Langmuir, B. Sarbas, and U. Nohl (2000), A global geochemical database structure for rocks, *Geochemistry, Geophysics, Geosystems*, *1*(5). https://doi.org/10.1029/1999GC000026

Magni, V., P. Bouilhol, and J. van Hunen (2014), Deep water recycling through time, *Geochemistry, Geophysics, Geosystems*, *15*(11), 4203-4216. https://doi.org/10.1002/2014GC005525

Matthews, K. J., K. T. Maloney, S. Zahirovic, S. E. Williams, M. Seton, and R. D. Müller (2016), Global plate boundary evolution and kinematics since the late Paleozoic, *Global and Planetary Change*, *146*(Supplement C), 226-250. https://doi.org/10.1016/j.gloplacha.2016.10.002

Miles, R. E. (1965), On Random Rotations in R^3, *Biometrika*, *52*(3/4), 636-639. https://doi.org/doi:10.2307/2333716

Müller, R. D., J. Cannon, X. Qin, R. J. Watson, M. Gurnis, S. Williams, T. Pfaffelmoser, M. Seton, S. H. J. Russell, and S. Zahirovic (2018), GPlates: Building a Virtual Earth Through Deep Time, *Geochemistry, Geophysics, Geosystems*, *19*(7), 2243-2261. https://doi.org/10.1029/2018GC007584

Parai, R., and S. Mukhopadhyay (2012), How large is the subducted water flux? New constraints on mantle regassing rates, *Earth and Planetary Science Letters*, *317–318*(0), 396-406. https://doi.org/10.1016/j.epsl.2011.11.024

Rüpke, L. H., J. P. Morgan, M. Hort, and J. A. D. Connolly (2004), Serpentine and the subduction zone water cycle, *Earth and Planetary Science Letters*, *223*(1–2), 17-34. https://doi.org/10.1016/j.epsl.2004.04.018

Sclater, J. G., C. Jaupart, and D. Galson (1980), The heat flow through oceanic and continental crust and the heat loss of the Earth, *Reviews of Geophysics*, *18*(1), 269-311. https://doi.org/10.1029/RG018i001p00269

Torsvik, T. H., B. Steinberger, G. E. Shephard, P. V. Doubrovine, C. Gaina, M. Domeier, C. P. Conrad, and W. W. Sager (2019), Pacific-Panthalassic Reconstructions: Overview, Errata and the Way Forward, *Geochemistry, Geophysics, Geosystems*, *20*(7), 3659-3689. https://doi.org/10.1029/2019gc008402

van Keken, P. E., B. R. Hacker, E. M. Syracuse, and G. A. Abers (2011), Subduction factory: 4. Depth-dependent flux of H2O from subducting slabs worldwide, *J. Geophys. Res.*, *116*(B1), B01401. https://doi.org/10.1029/2010jb007922

Wang, H. (2022), Hydrous regions of the mantle transition zone affect patterns of intraplate volcanism, *M.S. thesis, University of Oslo*, Oslo, Norway. https://www.duo.uio.no/handle/10852/96609

Zhong, S. J., M. T. Zuber, L. Moresi, and M. Gurnis (2000), Role of temperature-dependent viscosity and surface plates in spherical shell models of mantle convection, *Journal of Geophysical Research-Solid Earth*, *105*(B5), 11063-11082. https://doi.org/10.1029/2000jb900003

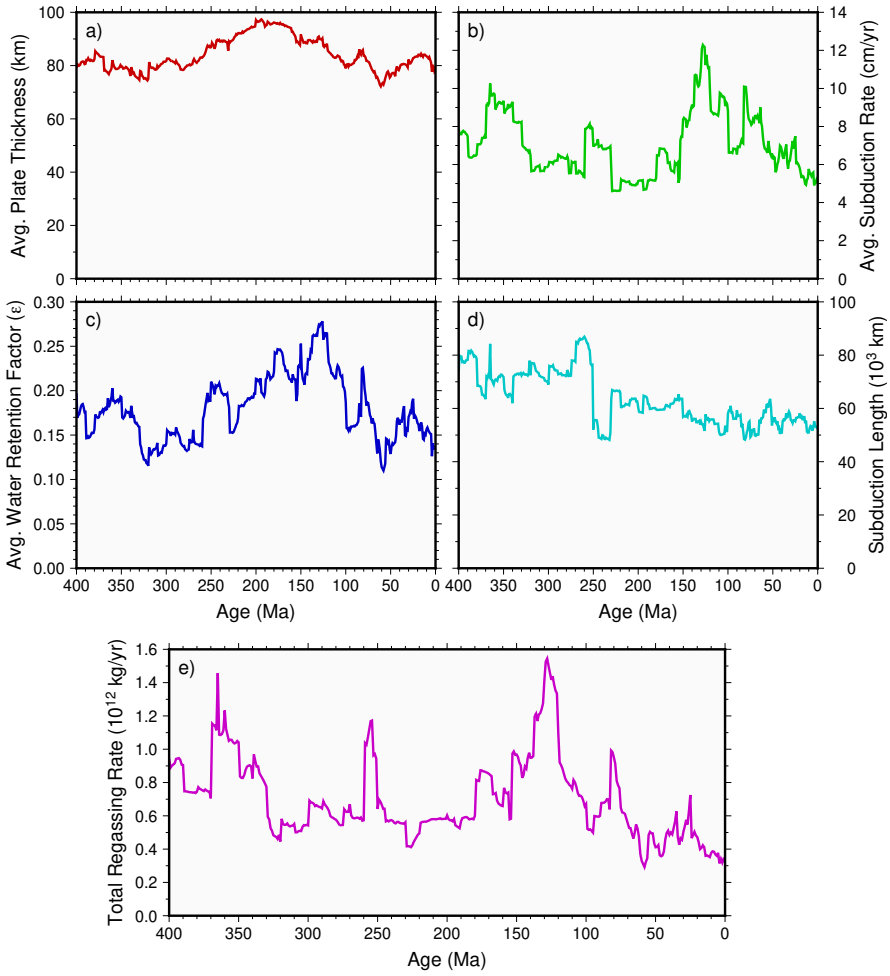

Figure S1. Parameters used to compute rates of regassing into the deep mantle, showing (a) the global average plate thickness, (b) the global average subduction rate, (c) the global average water retention fraction ε, and (d) the total length of global subduction zones. These parameters are combined using equation S2, as described in Supporting Information Text S1 to compute the regassing rate R [kg/m/year] along each subduction zone segment (main text Figure 2, left column). The summed regassing along all segments gives the (e) global total regassing flux, which varies significantly as a function of time since 400 Ma.

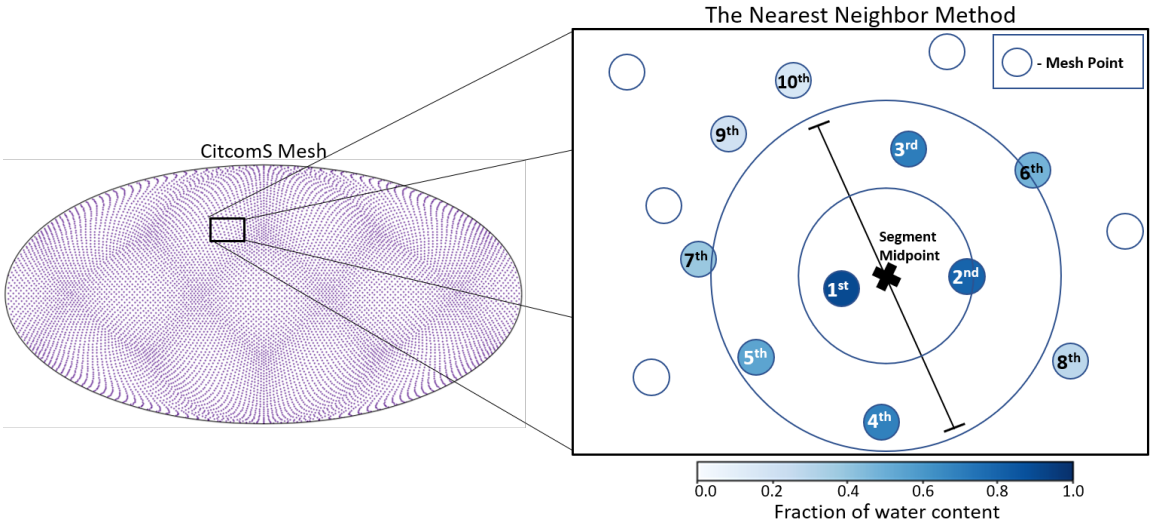

Figure S2. Assignment of water from a subduction zone segment onto mesh grid points. The left figure shows the global mesh point locations (purple, 10094 global mesh points positioned based on the CitcomS spherical finite element code [*Zhong et al.*, 2000]) using a Mollweide projection. In this grid, 12 diamond-shaped "caps" facilitate a relatively uniform distance between the mesh points on a spherical surface. On the right, an illustration of the nearest neighbor method shows a segment and its midpoint (marked with an X) and the *N* nearest neighbor mesh points (here, *N*=10). These points each receive a weighted relative fraction of the total water content (blue color, see equation S4) that is "regassed" to Earth's mantle at this segment midpoint. Grid points closer to the segment midpoint receive more water (darker blue), while more distant points receive less (lighter blue). Mesh points that are not among the *N* = 10 closest points to the segment midpoint do not receive any water (white).

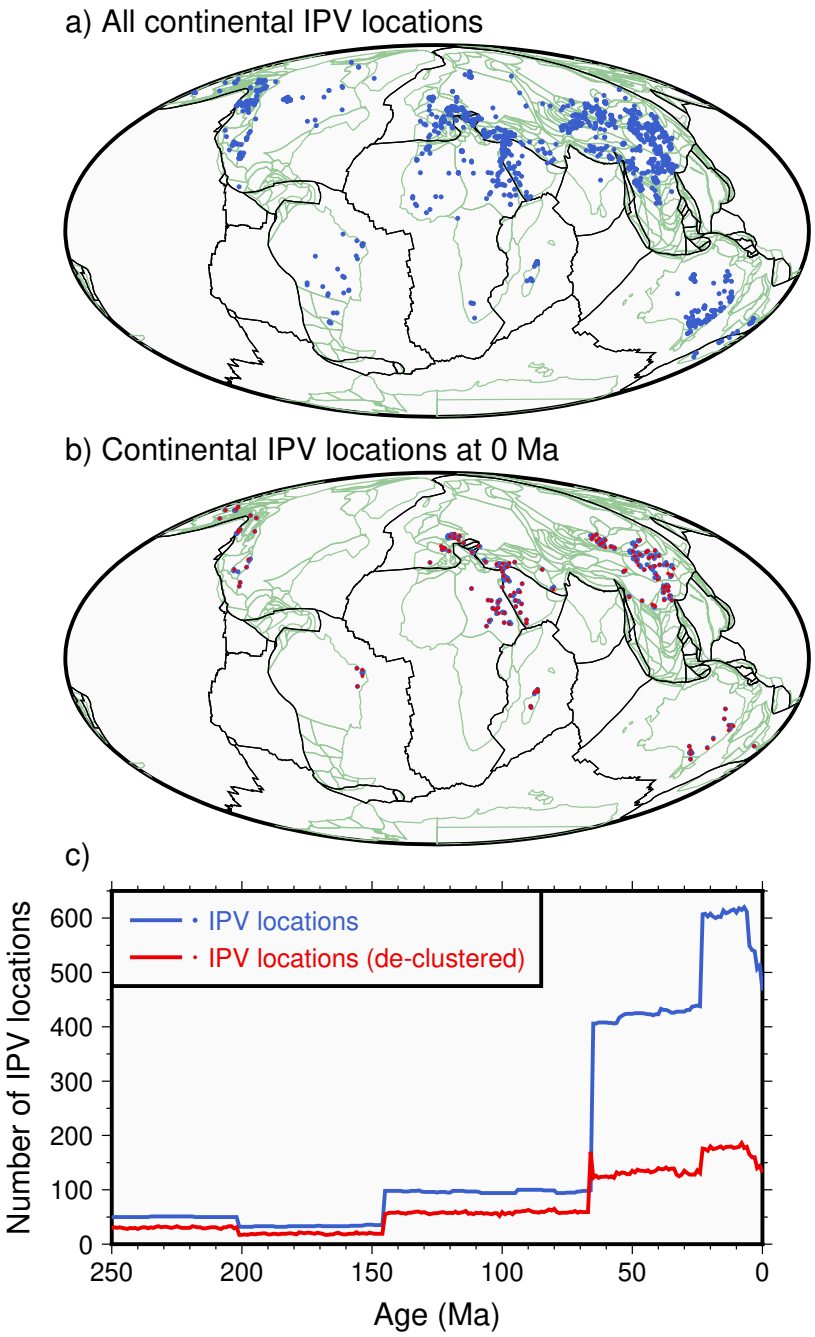

Figure S3. Continental intraplate volcanism (IPV) samples extracted from the GEOROC (https://georoc.eu/) database [*Lehnert et al.*, 2000]. Shown in (a) are the 2095 continental IPV locations with eruption ages between 0 and 250 Ma (blue dots). Shown in (b) are the 467 continental IPV locations with 0 Ma age (blue dots), which define 132 IPV locations after de-clustering (red dots, see Supporting Information Text S3). Shown in (c) are the number of different IPV locations as a function of age between 250 and 0 Ma, both for all IPV locations (blue line) and for the de-clustered locations (red line).

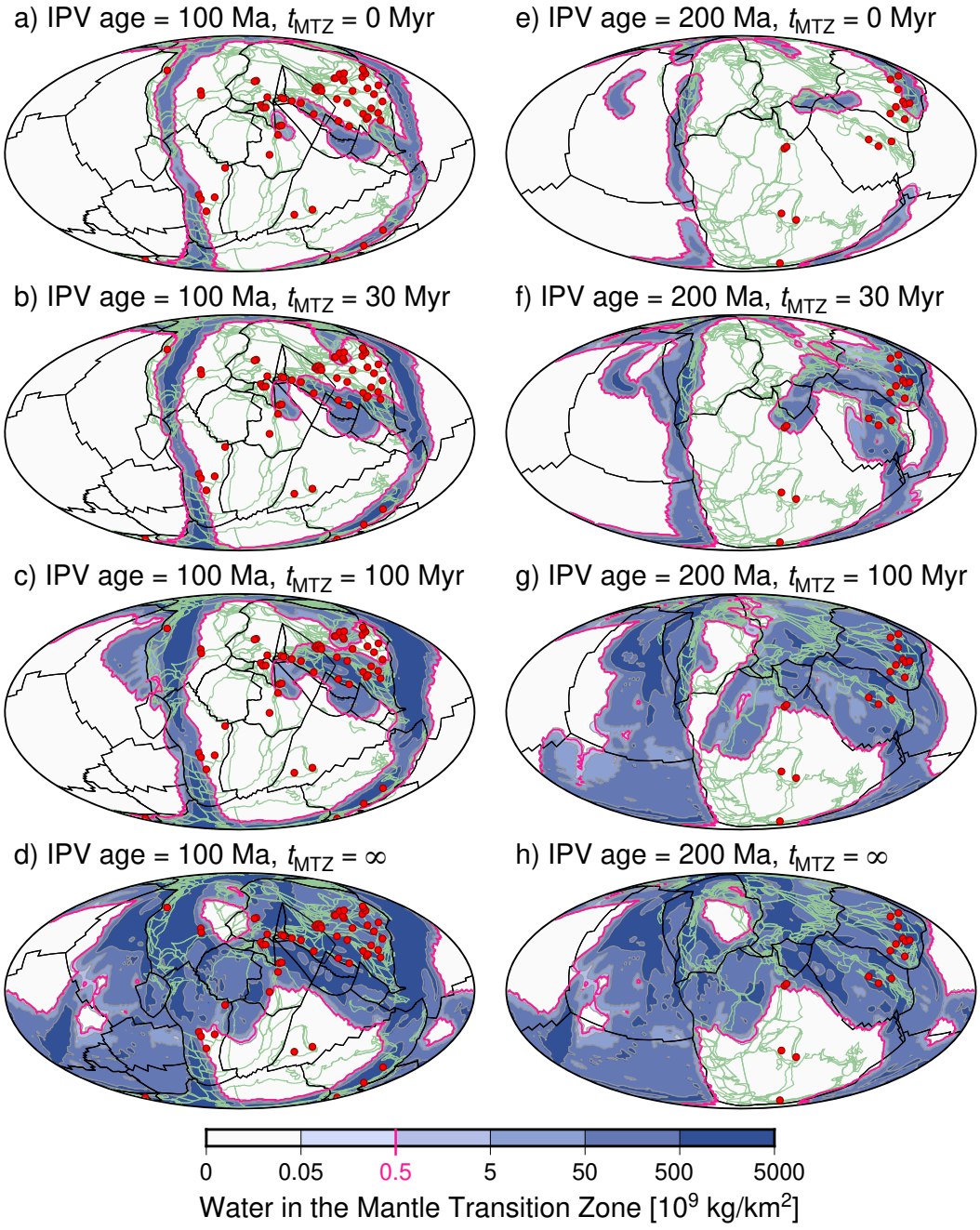

Figure S4. Effect of varying MTZ water residence time, shown at 100 Ma (left column, a-d) and 200 Ma (right column, e-h). Predictions of the water distribution in the mantle transition zone (MTZ) are shown using colors (as for Figure 3 of the main text), with locations of active continental intraplate volcanism (IPV) shown by red dots. The slab sinking rate is v_{sink} = 3 cm/yr, and there is a t_{IPV} = 20 Myr IPV delay. The MTZ water residence time is (a, e) t_{MTZ} = 0 Myr, (b, f) t_{MTZ} = 30 Myr, (c, g) t_{MTZ} = 100 Myr, and (d, h) t_{MTZ} = ∞, meaning that water that reaches the MTZ stays there.

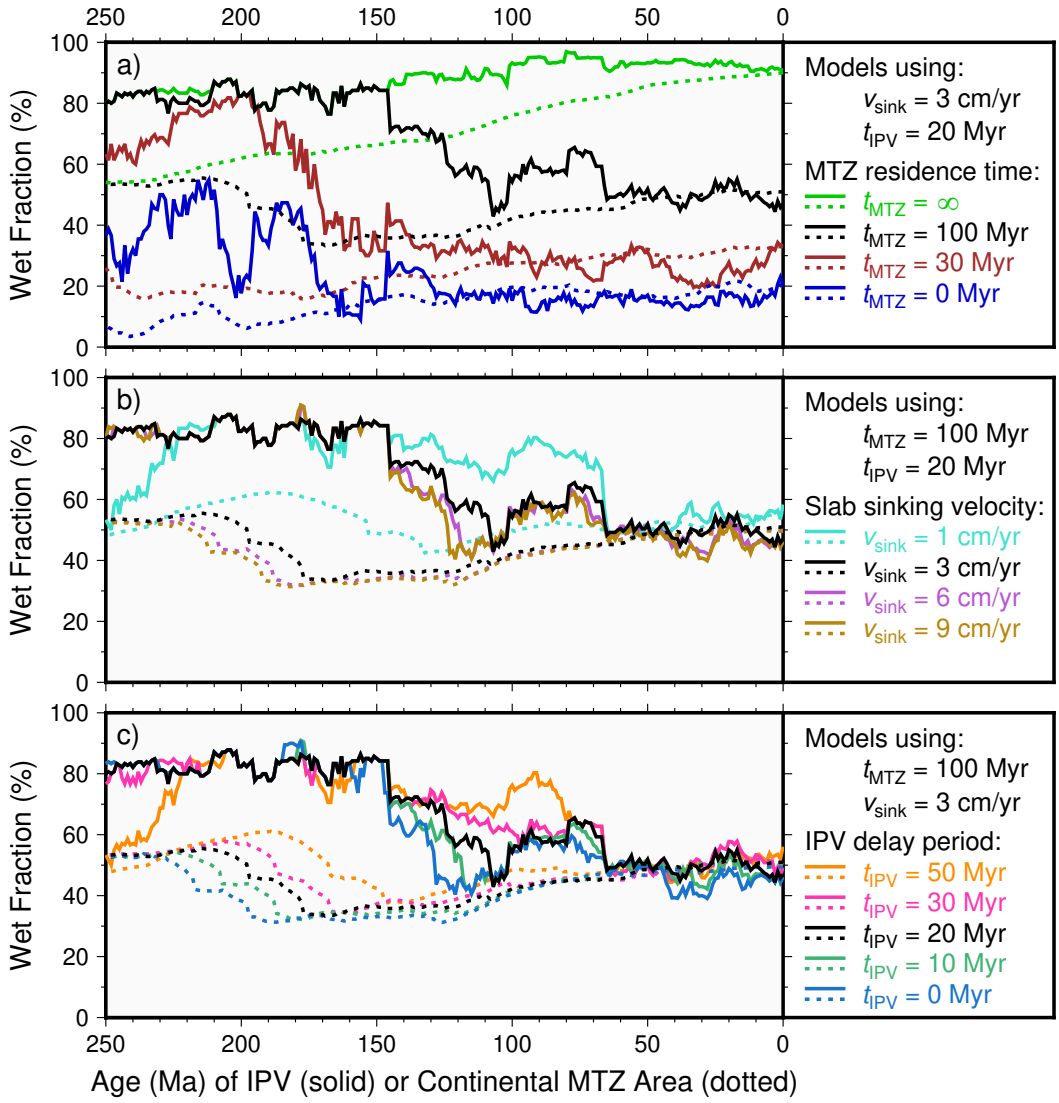

Figure S5. The fraction of continental IPV locations and continental areas sitting above hydrated MTZ for different scenarios. Similar to Figure 5 of the main text, except that dotted lines show the fraction of continental areas (instead of global areas for the dashed lines in main text Figure 5) that sit above hydrated MTZ. Black lines reproduce the lines in Figure 3g of the main text, i.e., the reference scenario.

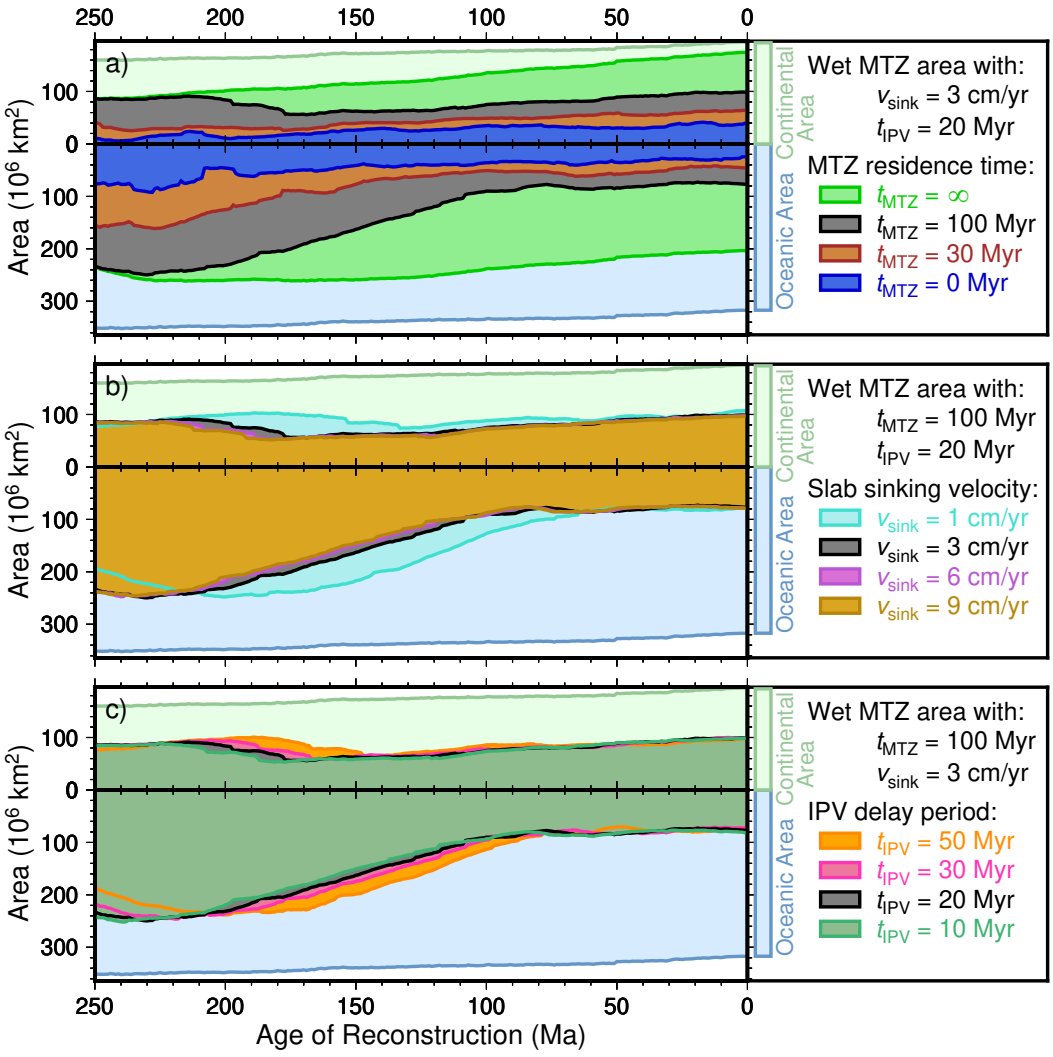

Figure S6. The area of continental and oceanic regions sitting above hydrated MTZ for different scenarios. Shown are the total areas of the continents (light green area) and oceans (light blue area) as a function of time through the reconstruction, and the portions of these areas that sit above hydrated MTZ (shown by the darker colored areas, which represent the different models from the corresponding panels of main text Figure 5, and described by the legends on the right). In each panel, continental and oceanic areas are shown above and below the x-axis, respectively. The black lines surrounding grey areas are for the reference scenario, and are the same in each panel.

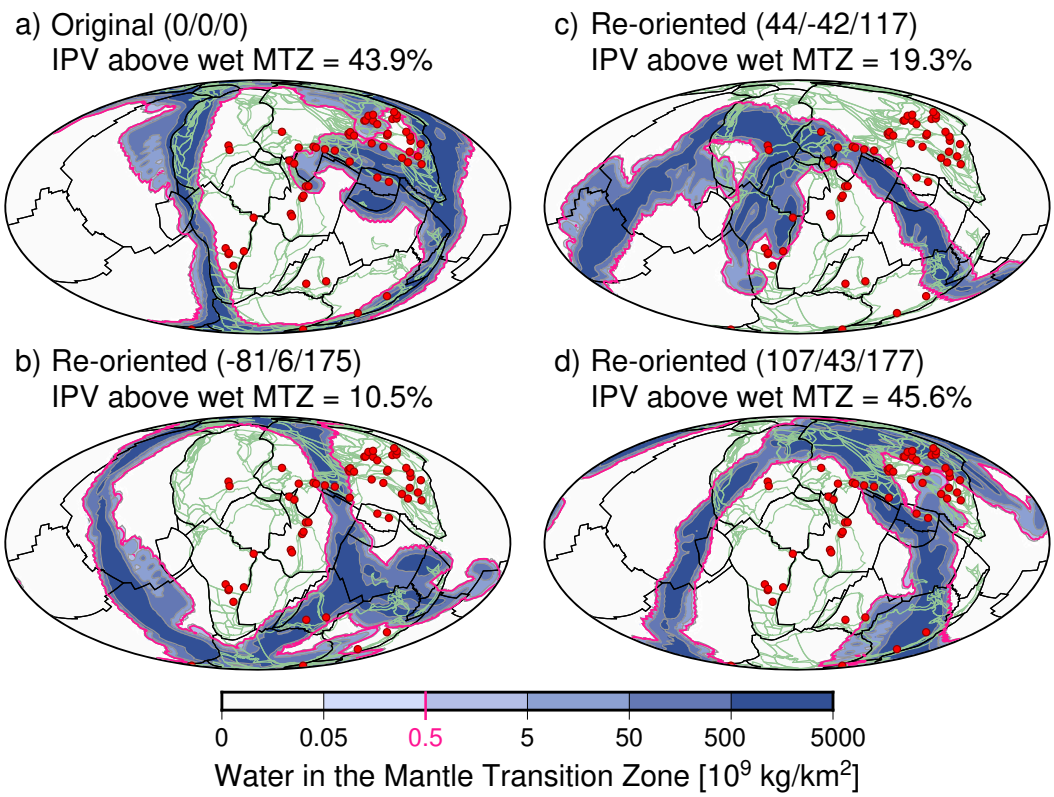

Figure S7. Examples showing the re-orientation of the MTZ water grid. The illustration displays the mantle transition zone (MTZ) water grid at 125 Ma with an MTZ water residence time of t_{MTZ} = 100 Myr, a slab sinking rate of v_{sink} = 3 cm/yr, and IPV delay period of t_{IPV} = 20 Myr, i.e., the reference scenario of this study. Shown are the original grid (a) and three re-orientations of this grid (b-d) as defined by random choices of longitude/latitude/rotation (above each figure, in degrees). Stationary locations of continental intraplate volcanism (IPV) (red dots), reconstructed continental blocks (green lines), and plate boundaries (black lines) are also displayed (these are not rotated with the MTZ water grid). The percentage of continental IPV samples above wet MTZ values (i.e., ≥ 0.5 ·10^9 kg/km^2, pink contour) are given for each water grid rotation.